Journal of The Electrochemical Society

Identification of the Underlying Processes in Impedance Response of Sulfur/Carbon Composite Cathodes at Different SOC

Journal of The Electrochemical Society, 2022 **169** 030505

Identification of the Underlying Processes in Impedance Response of Sulfur/Carbon Composite Cathodes at Different SOC

Martina Gerle,[1] Norbert Wagner,[1] Joachim Häcker,[1] Maryam Nojabaee,[1,z] and Kasper Andreas Friedrich[1,2,*]

[1]*German Aerospace Center (DLR), Institute of Engineering Thermodynamics, 70569 Stuttgart, Germany*
[2]*University of Stuttgart, Institute for Building Energetics, 70569 Stuttgart, Germany*

For lithium-sulfur batteries, porous carbon/sulfur composite cathodes are the primary solution to compensate the non-conductive nature of sulfur. The composition and structure of this class of cathodes are crucial to the electrochemical performance, achieved energy density and the stability of the cell. Electrochemical impedance spectroscopy is employed to investigate and correlate the electrochemical performance of lithium-sulfur batteries to the composition and microstructure of differently fabricated carbon/sulfur composite cathodes. A transmission line model is applied to identify different underlying electrochemical processes appearing in the impedance response of a range of porous carbon/sulfur cathodes. The integration of a lithium ring serving as a counter electrode coupled with advanced wiring has allowed an artifact-free recording of the cathode impedance at different states of charge with the aim to investigate the evolution of impedance during discharge/charge and the kinetics of charge transfer depending on the infiltration method and the utilized carbon host. It is shown that impedance response of this class of cathodes is highly diverse and the plausible underlying processes are discussed in details. To this end, quasi-solid-state and various polysulfide-based charge transfer mechanisms are identified and their time constants are reported.
 [DOI: 10.1149/1945-7111/ac56a4]

Manuscript submitted November 13, 2021; revised manuscript received January 18, 2022. Published March 3, 2022. *This paper is part of the JES Focus Issue on Women in Electrochemistry.*

Supplementary material for this article is available online

Lithium-sulfur (Li-S) cells surpass lithium-ion batteries (LIB) in gravimetric energy density, delivering up to 470 Wh kg^{-1}, thereby yielding an attractive alternative for aerospace and heavy-duty applications.[1,2] The low cost and high availability of sulfur (S) are additional advantages that favorably contribute to the cell cost and sustainability of the system. However, the deployment of batteries in such demanding applications mandates a compelling cycle life, which is one of the major challenges the Li-S system faces. The lithium (Li) metal anode-related instabilities, polysulfide (PS) shuttle phenomena and cathode-induced limitation factors are among parameters suppressing the cyclability of these batteries.[3,4] Regarding the latter, critical issues such as the isolating character of S limiting the active material percentage, the significant volume expansion caused by the conversion reaction of S_8 to Li_2S_2/Li_2S as well as sluggish charge transfer (CT) kinetics stemmed from deposition of Li_2S on the composite cathode are remained to be solved.[5–8] To address these challenges, highly porous carbon (C) materials are commonly employed in composite cathodes for Li-S batteries influencing not only the conductivity of the cathode, but also the diffusion and charge transport processes as well as PS retention.[9–12] The composition and structure of this class of cathode are crucial to the electrochemical performance, the achieved energy density and the stability of the cell.[13] Specifically, the volume and size distribution of the pores in the C host were demonstrated to be crucial to the capacity retention.[14–16] The employment of microporous C enabling S confinement via melt or gas infiltration has been studied in detail in both ether and carbonate-based electrolytes.[17–19] Therein, quasi-solid-state reaction (QSS; direct conversion of S_8 to Li_2S_2/Li_2S) was identified for composite cathodes using microporous C.

To investigate and correlate the electrochemical performance to the composition and microstructure of the composite cathode, several techniques such as optical operando methods, including Raman, infrared, UV–vis spectroscopy and XRD have been developed and implemented.[20–25] Among electrochemical methods, impedance spectroscopy (IS) has been established to study cathode- and electrolyte-related processes and limiting factors in Li-S cells.[14,26–28] In addition to the full cell implemented by Canas et al. and the 3-electrode (3E) setup employed by Qiu et al., in a more recent attempt Walus et al. adopted the symmetrical cell reassembled using two previously cycled electrodes to exclude the contribution of the anode-related processes to the impedance.[29,30]

In the study presented here, with an objective to eliminate the challenges of electrochemical impedance spectroscopy (EIS) in 3E setup such as distortion and induction loops and at the same time avoiding the complications arising from opening and reassembling the symmetrical cell,[31–33] an upgraded configuration with an integrated Li ring serving as the counter electrode is implemented which enables recording the symmetrical cathode EIS at different states of charge (SOCs)/depths of discharge (DODs). Furthermore, the transmission line model (TLM) characteristics of the porous electrode, which has been widely used to describe the impedance of the electrodes in Li-ion battery systems but not fully adopted for the S composite cathode, is used and discussed in detail within this work. The classical TLM developed by De Levie[34,35] and further detailed by Bisquert[36,37] consists of two channels connected by a transition part. The upper channel describes processes inside the pore, e.g. resistance for ions confined in the electrolyte-filled pores while the lower channel is assigned to processes within the electrode material. The connecting transition part addresses the processes at the interface, e.g. CT reactions. Adamič et al. employed the TLM to simulate the impedance response of the PS catholyte-based system with a C cathode.[38] Therein, the conventional TLM is upgraded considering the additional diffusion of counter ions in the pores of the electrode which is coupled to the diffusion in the separator. In a further extension to this work, Drvarič-Talian et al. employed the TLM to describe the potential interaction of both active and counter-ions with two different electrodes at each end of the transmission enabling the simulation of the full-cell impedance.[39]

In the present study the attempts are rather devoted to the composite C-S cathode and the porous behavior associated with such a structure. The intention hereby is to establish a firm knowledge about the different electrochemical processes stemming from the structural properties of the cathode by employing the range of C-S

*Electrochemical Society Member.
[z]E-mail: maryam.nojabaee@dlr.de

composite cathodes using an accessible technique namely EIS. To this end, C materials offering different porosity including mesoporous Ketjenblack (KB) and microporous carbon aerogel (CA) with different pore sizes have been investigated. Using a suitable TLM, the resistance of bulk and pore electrolyte, inter-particles, and CT are identified and quantified. Additionally, the effect of different S-infiltration methods such as gas and mechanical mixing on the evolution of impedance upon discharge/charge in the first formation cycle is tackled. The reflection of different CT mechanisms corresponding to the various redox reactions in the impedance spectra of the cathode is identified and the respective kinetics are discussed elaborately, whereby it is shown how the infiltration method correlated to the porosity of the C material leads to distinct CT pathways and kinetics.

Experimental

Cathode preparation and characterization.—Commercially available KB EC-600 JD (Akzo Nobel) representing mesoporous C and synthesized CAs as an example of microporous C along with S powder (99.5%, Alfa Aesar) are used for preparation of the composite cathodes. The pore size distributions of the employed C host materials are depicted in Fig. S1 (available online at stacks.iop.org/JES/169/030505/mmedia). Detailed information on synthesis route of the CAs can be found in our previous publication.[17] Thereby, the CAs densities and porous structure can be configured by the use of certain reagents, such as Ar, CO_2 or N_2. Different preparation methods, i.e. mechanical mixing and gas infiltration, are undertaken to prepare C/S composites. Firstly, a non-infiltrated, mixed C/S composite was fabricated by ball-milling the S and C components for 15 min at 700 rpm. C/S mixtures with ratios of 7:3 and 3:7 were prepared to allow further comparisons with regard to the active material percentage. Moreover, gas S-infiltrated cathodes were fabricated via the application of heat treatments in order to incorporate the S into the porous C structure. Thereby the ball-milled C/S mixture was heated at 600 °C for 6 h for gas infiltration.[17] In order to remove remaining non-infiltrated surficial S, the infiltrated C/S compounds were treated with a second heating process step in a tube furnace by heating up to 200 °C and holding for 12 h.

Subsequently, an aqueous slurry was prepared by mixing the C/S composites with the binders CMC (carboxymethyl cellulose, Walocel CRT 2000 PA, Dow Wolff) and PEO (polyethylene oxide, M_V = 600 000, Sigma Aldrich) at a weight ratio of 90:3:7 (C/S: CMC: PEO) in a tumbling mixer. After mixing, the homogenous slurry was doctor-bladed with different coating thicknesses on a C-primed aluminum foil. The full list of the herein prepared cathodes can be found in Table SI (see supplementary).

Cell assembly.—All measurements were conducted in ECC-PAT-Core cells (EL-CELL) with a symmetrical 2E or 3E setup. The cells were assembled in an argon-filled glovebox (Jacomex GPTFF, < 1 ppm H_2O, < 3 ppm O_2). For a 2E setup, two identical C/S cathodes were separated by a GF/C glass fiber sheet (Whatman, 21.6 mm diameter, 260 μm thickness). As electrolyte, 160 μl ether-based DOL/DME electrolyte containing 1 M Lithium bis(trifluoromethanesulfonic)imide (LiTFSi) conducting salt (Alfa Aesar) was added. To enable measurements at various SOCs/DODs, a Li reference ring with a thickness of 0.6 mm, 19 mm inner and 21.6 mm outer diameter was utilized as third electrode/anode. Prior to each measurement, the cells underwent a rest time of 1 h to allow proper wetting of the separator and the porous electrodes in order to reach steady state conditions.

Electrochemical impedance spectroscopy and galvanostatic cycling.—EIS measurements were performed using a Zahner IM6 and ZENNIUM Pro workstation. All measurements were conducted in potentiostatic mode in a frequency range from 5 MHz to 100 mHz with an amplitude of 10 mV. In addition to the impedance measurements at the OCV, EIS evolution at different SOCs or rather DODs were investigated. Therefore, a 3E cell configuration with Li metal reference ring serving as anode was utilized. To allow automatic impedance measurements at specified cycling states, the battery cycling system BaSyTec and the Zahner impedance measurement setup were combined, see Fig. S2. Therefore, an advanced wiring of the test cell was necessary on the hardware side. The connection on the software side was implemented by a Raspberry Pi single-board computer, which connects both systems and has access to a database specifying the impedance measurement conditions. For all SOC/DOD related impedance measurements the same test plan and the same impedance measuring properties as described before were applied. Before discharging the cells, a prolonged resting period of at least 5 h with hourly impedance recording steps was included to the test plan.

Discharging/charging was performed at C/10 in between the cut-off voltages 3.5 V and 1 V with intermediate EIS measurements at equidistant capacity steps of 1/10 of the theoretical capacity. A resting time of two hours was included between every discharge/charge step and the subsequent EIS measurement, as equilibrium conditions are crucial to exclude non-linear effects on impedance spectra.

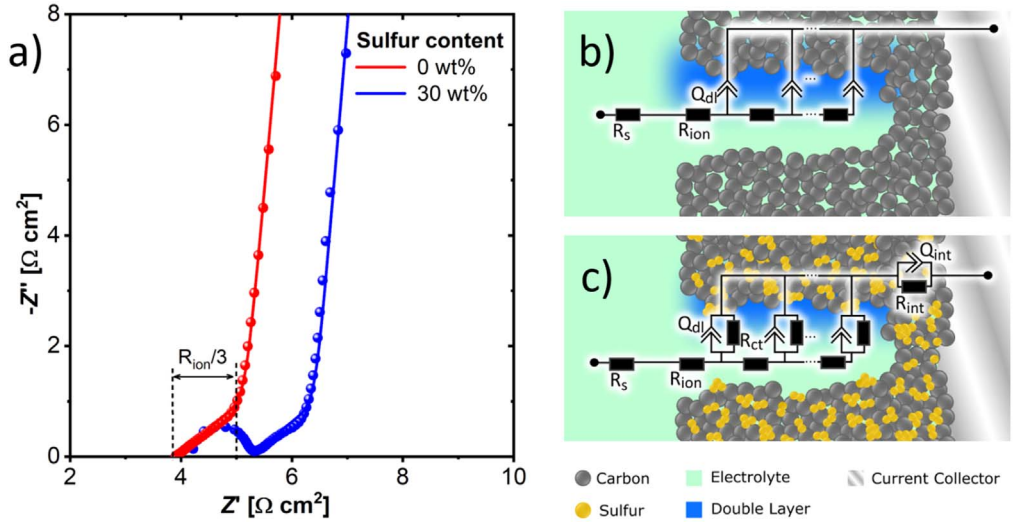

Figure 1. (a) Nyquist presentation of OCV impedance of S-free and S-containing KB cathodes; scatter: measured data; line: fitting result (b) TLM used for fitting for non-S cathodes in OCV; (c) expected TLM for S-containing cathodes in OCV. However, better fits are achieved using blocking EC.

Examination, modelling and fitting of the recorded spectra were performed with the stand-alone impedance analysis software RelaxIS3 (rhd instruments). Previous to fitting, the quality of the measured data was verified using Kramers-Kronig[40] transformation. The quality of the obtained fitting values and the suitability of the used equivalent circuit model was evaluated with various quality criteria, such as Chi-square, residual analysis and mathematical error values for single fitting parameter which are shown/mentioned as error bars. Furthermore, DRT analysis was applied (using RelaxIS3 software) wherever necessary to distinguish the overlapping processes.

Results and Discussion

Impedance response at the open circuit voltage.—The characteristic Nyquist plots of symmetrical 2E cells comprising two cathodes of pure KB (KB_{pure}, red line) and mixed KB/30 wt% S cathodes ($KB/S_{mixed,30}$, blue line) are shown in Fig. 1a. In case of pure C, the typical blocking response of the porous electrode (in the absence of the faradic reaction at the surface) is recorded, which is manifested in the Nyquist diagram in a 45° incline in the middle frequency (MF) region characteristic for the resistance of ions within the pores (R_{ion}) followed by a straight line with an angle of almost 90° featuring the blocking behavior due to the absence of active material. Latter is described with Q_{dl}, a constant phase element (CPE), characterizing the local charge accumulation and double layer formation at the interface. The equivalent circuit (EC), depicted in Fig. 1b, is adopted to fit the experimental data for this sample which is comprised of a blocking TLM describing the aforementioned processes in series with a resistance (R_s) attributed to the ohmic response originating mainly from the electrolyte. The overall impedance (Z) hereby is calculated using Eq. 1:

$$Z = R_s + \left[\frac{R_{ion}}{Q_{dl}(j\omega)^{\alpha}}\right]^{\frac{1}{2}} \cdot \coth\{L[R_{ion}\cdot Q_{dl}(j\omega)^{\alpha}]^{1/2}\} \quad [1]$$

where ω is the angular frequency of the excitation signal and L the pore length in the porous electrode. The extent of the x-axis intercept corresponds to 1/3 of the ionic resistance in the pore. Of note, the blocking condition appears non-ideal due to parasitic reactions such as the formation of a passivation layer on the blocking electrode. This indeed leads to a deviation of the R_{ion} values measured by the above-mentioned analysis from the true values. Therefore the reported R_{ion} values should be considered as apparent rather than the true values.[41]

An additional process can be distinguished for an active-material containing cathode: a semicircle $(RQ)_{int}$ at high frequencies (HF; 0.1 MHz $\leqslant f \leqslant$ 1 MHz) assigned to the interparticle effects of the electrical network of the composite electrode,[43–45] shown in Fig. 1c. Surprisingly, the composite electrode appears to be blocking despite the presence of the active material at the OCV. This is due to the relatively small excitation (10 mV) at OCV potentials. Since the CT reactions cannot be fully excluded given the presence of S, a non-blocking TLM is expected. In this case the impedance is given by Eq. 2:

$$Z = R_s + [R_{ion}\cdot\zeta]^{1/2}\ \coth\left[L\left(\frac{R_{ion}}{\zeta}\right)^{1/2}\right] \quad [2]$$

with

$$\zeta = \left[\frac{1}{R_{ct}} + Q_{dl}(j\omega)^{\alpha}\right]^{-1} \quad [3]$$

This yields extremely large CT resistances (R_{ct}) values which mathematically, as shown in Eqs. 4 and 5, equals the impedance of the blocking electrode.

$$Z_{(RQ)} = \frac{1}{\frac{1}{Z_{Rct}} + \frac{1}{Z_{Qdl}}} = \frac{1}{\frac{1}{R_{ct}} + Q_{dl}(j\omega)^{\alpha}} \quad [4]$$

$$Z_{(RQ),R\to\infty} = \frac{1}{0 + Q_{dl}(j\omega)^{\alpha}} = Z_{Qdl} \quad [5]$$

Impedance evolution upon first discharge/charge.—In order to identify the potential physical as well as the underlying chemical and electrochemical processes occurring in the impedance behavior of C/S composite cathodes during cycling, three differently fabricated composite cathodes ($CA(Ar)/S_{gas}$, $KB/S_{mixed,30}$ and $CA(Ar)/S_{mixed,30}$) are considered as model systems. In particular, these case studies represent the typical galvanostatic cycling characteristics and the occurring redox reaction mechanism in a Li-S cell reported in literature.[17,42]

Figure 2 summarizes these plausible voltage profiles depending on the porosity of the C host material as well as the employed infiltration method. As explained in the introduction section, infiltration and anchoring of active material into the UMC host material alters the nature of the occurring CT mechanisms, whereby the voltage profile and the potentials of the characteristic discharge and charge plateaus adopt accordingly as shown in Fig. 2a. For the $CA(Ar)/S_{gas}$ cathode, a distinct discharge plateau around a considerably lower potential of 1.6 V can be observed corresponding to the QSS-CT reaction of $S_{8,\ polymorph} \rightarrow Li_2S$ (QSS-CT).[16,18] In addition to the expected long plateau at 1.6 V, a negligible plateau around 2.1 V is visible at the beginning of the discharge region, pointing that the dissolution of the remaining surficial S has proceeded to a small extent. In contrast to this, upon charge a second (2.3 V) and third (2.4 V) plateau corresponding to the $S_4^{2-} \rightarrow S_8^{2-}$ ($PS\text{-}CT_1$) and $S_8^{2-} \rightarrow S_8$ ($PS\text{-}CT_2$) oxidation reactions can be observed in addition to the oxidation step of QSS-CT (at 1.8 V). This leads to dissolution of PS and irreversible capacity upon first cycle in such systems.[17] The main reason for the appearance of this oxidation

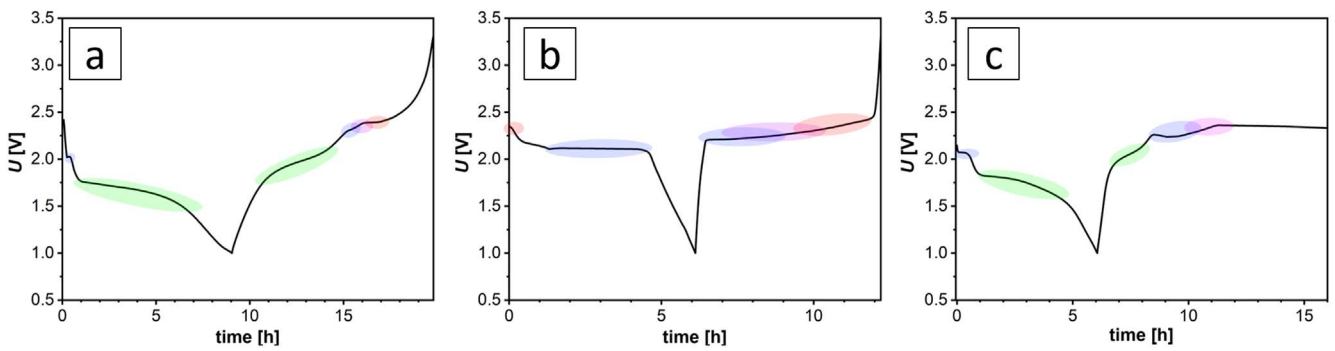

Figure 2. Characteristic voltage plateaus of cathodes with different material systems: (a) $CA(Ar)/S_{gas}$; (b) $KB/S_{mixed,30}$; (c) $CA(Ar)/S_{mixed,30}$.

steps upon charge is the formation and dissolution of semisolid Li_2S_4 upon oxidation of Li_2S.[43]

Figure 2b depicts the recorded voltage profile of a cell with KB/$S_{mixed,30}$ cathode. As KB consists of solely mesopores and no thermal infiltration process was carried out, the voltage profile upon discharge shows the characteristic plateaus corresponding to the PS-based CT mechanisms (solid-liquid-solid) around 2.3 V and 2.1 V attributed to the reduction steps of $S_8 \rightarrow S_8^{2-}$ (PS-CT_2) and $S_4^{2-} \rightarrow Li_2S_2/Li_2S$ (PS-CT_3), respectively.[44,45] Upon charge, corresponding plateaus for the oxidation reactions of $S_4^{2-} \rightarrow S_8^{2-}$ (PS-CT_1) and $S_8^{2-} \rightarrow S_8$ (PS-CT_2) steps can be observed at 2.3 V and 2.4 V, respectively. Additionally, the initial oxidation step of $Li_2S_2/Li_2S \leftrightarrow S_4^{2-}$ (PS-CT_3) arising at the very beginning of the charge process and leading to a sharp incline, is expected to be still active within the 2.3 V plateau due to sluggish charge transfer kinetics of solid Li_2S/Li_2S_2 oxidation.[46] The foregoing discussion is for simplification and does not exclude the formation of S_6^{2-}, the $S_3^{\cdot-}$ radical and correspondingly the intermediary reaction steps, e.g. the discharge reactions such as $S_8 \rightarrow S_8^{2-} \rightarrow S_6^{2-}(S_3^{\cdot-})$ and $S_4^{2-} \leftrightarrow S_6^{2-}(S_3^{\cdot-})$ as well as the charge reaction of $S_6^{2-} \rightarrow S_8$.[42] In contrast to these two samples, both CT mechanisms, i.e. QSS-CT and PS-CT, are observed for the CA(Ar)/$S_{mixed,30}$ sample as depicted in Fig. 2c, resulting from elemental S_8 on the C surface as well as $S_{8,polymorph}$ species protected by the micropores.[47] The charge process for this sample appears to face a strong PS-shuttle whereby the full oxidation to higher potentials is hindered.

Herein, the in-situ impedance data was recorded at defined DODs/SOCs during the first discharge/charge cycle for these three cathode materials in order to gain a broader understanding on the underlying mechanisms and kinetics of the CT mechanisms. Therefore, a symmetrical configuration consisting of two C/S cathodes and a Li reference, serving as the anode, was implemented. The charge/discharge profile recorded for such cell design was compared to a 2-electrode (2E) setup to ensure the elimination of the originated geometrical effect from the 3E cell setup, see Fig. S3.

The capacity, efficiency and long-time cycling performance of these various systems has already been investigated in detail in one of our previous studies.[17] As evident from Fig. S4a, the infiltration and anchoring of the active material within the UMC carbon host indeed exhibits the highest specific capacity and most stable long-term cyclability. For mixed CA(Ar)/S and KB/S cells however, lower and slowly decaying performances are found due to their tendency to side reactions and PS-shuttle effect, as discussed above.

Gas infiltrated CA(Ar)/S.—In Fig. 3a, the recorded discharge/charge profile of a full cell in 3E setup with CA(Ar)/S_{gas} cathodes is depicted. A prolonged OCV-phase of 50 h was chosen in order to investigate undesired effects such as self-discharge upon relaxation period. The colored dots mark the recordings of impedance data. The voltage peaks at the EIS measurement points can be attributed to the relaxation breaks, which are not depicted in the plateaus.

Figure 3b shows the corresponding EIS spectra at different DODs. At the OCV state (0% DOD, measurement 0), the impedance spectrum of the cell exhibits the same characteristics as observed in previous OCV investigations for mixed electrodes, i.e. a blocking response in the LF region, an inter-particle response in the HF area and the ionic pore resistance in between. Indeed, the impedance remains unchanged after relaxation, implying that the self-discharge reactions are suppressed by entrapment of the active material. Interestingly upon discharge initiation, a remarkable change in the LF section with an emerging semicircle is recorded. The LF branch with appendant semicircle decreases during progressing along the 1.6 V plateau and further until the end of the discharge process. The observed semicircle is attributed to the QSS-CT mechanism $(RQ)_{QSS\text{-}CT}$. The spectra recorded for 8%–72% DOD are fitted with the EC shown in Fig. 3c. With further discharge, R_{ct} decreases and an additional branch appears in the LF range for deeper DOD (72%–100% DOD, measurement 9–13), describing a nearly infinite diffusive process i.e. the solid diffusion of Li-ions fitted using Q_{diff} (see the EC in Fig. 3d). To make sure the low branch is corresponding to the diffusion but no other CT processes, the EIS of a fully discharged cell is recorded up to ultra-low frequencies (32 μHz), see Fig. S5. Distribution of relaxation times (DRT) analysis was employed to carry out a more precise classification of the identified processes with respect to the corresponding frequency ranges as well as the relaxation times, see Fig. 3e. In addition to the R_{ct}, the evolution of R_s, R_{ion} and R_{int} is explored, see Fig. 3f. Interestingly, R_s remains almost unchanged at 1.5 Ω upon discharge process. This steady behavior can be attributed to the lack of PS dissolution in the bulk electrolyte as a consequence of the QSS-CT. The formation of PSs is shown to increase the viscosity of the electrolyte, resulting in a higher resistance.[48] For the presented system however, since the trapped S in the micropores is not dissolved in the electrolyte, no substantial viscosity changes in the electrolyte and thus no significant resistance alteration arises in the further discharge steps. Similar trend is observed for the R_{ion} at the OCV as well as early DODs due to the same reason. At the deeper DOD however R_{ion} increases steadily due to the consumption of Li-ions in the pores and the local depletion in the concentration of the ionic carriers, and consequential reduction in pore ionic conductivity. Such an effect is not observed for the bulk, where the depletion of the cation is compensated fast enough from the anode during discharge. In the case of R_{int}, a stable value can be noted before plateau. Afterwards R_{int} keeps falling explainable by the higher ionic conductivity of the solid product Li_2S/Li_2S_2 ($\sigma_{Li2S} = 1{\cdot}10^{-17}$ S cm^{-1} [49]) relative to elemental S ($\sigma_{S8} = 5{\cdot}10^{-30}$ S cm^{-1} [50]). Interestingly, after the plateau (from 1.5 V to 1 V) R_{int} begins to increase again, as eventually the Li_2S precipitation overlies the surface of the conductive C material, also in corroboration with rerise of the R_{ion} after plateau.

For the charging process shown in Fig. 4a at the earlier states, in addition to the interparticle reaction and the ionic pore resistance, the QSS-CT semicircle and the LF branch representing solid diffusion are distinctly evident. At higher SOCs (>70% SOC), different impedance responses are identified, see Fig. 4b. Considering the voltage profile, the second plateau at 2.3 V linked to the oxidation step of $S_4^{2-} \rightarrow S_8^{2-}$ (PS-CT_1) arises at about 70% SOC. This naturally faster PS-CT reaction (relative to QSS-CT) is emerging at higher frequencies. In the last EIS spectrum recorded at 100% SOC, a semicircle becomes ultimately fully visible in the MF region. With regard to the position in the voltage plateau, this response conforms the oxidation of long-chain PSs to solid S, $S_8^{2-} \rightarrow S_8$ (PS-CT_2). Apparently, this process and the ionic pore response share similar relaxation times, the 45° incline is superimposed by the oxidation reaction disabling the application of the TLM. Instead, a serial connection of two (RQ)-circuit elements is assigned to inter-particle effects $(RQ)_{int}$, oxidation to solid S ($S_8^{2-} \rightarrow S_8$, $(RQ)_{PS\text{-}CT2}$) as well as the CPE element Q_{diff} describing the solid diffusion, see Fig. 4c. The evolution of other resistances upon charge is shown in Fig. S6. The series resistance, which originates mostly from the electrolyte, steadily increases from 1.5 V to 1.9 Ω. The reason therefore is the mentioned second oxidation step forming semisolid Li_2S_4 which results in further dissolution to PS. This agrees with the maximum R_s appearing at the end of the second charge plateau. Furthermore, an increase of R_{ion} can be observed within the second half of the charge process which is in accordance with the overall rise of the R_s. Since the inter-particle resistance R_{int} is not falling but slightly growing during charging of the cell, it is evident that the effect of the cathode passivation occurring due to Li_2S_2/Li_2S formation at the end of the discharge process is indeed irreversible.

Mixed KB.—In contrast to the CT processes identified for gas infiltrated CA(Ar)/S cathodes, pure PS-CT mechanism was observed in the mesoporous C host system mixed with S (KB/$S_{mixed,30}$). As expected, two characteristic PS-based discharge plateaus at 2.3 V and 2.1 V can be noticed, see Fig. S7. Recorded EIS spectra for this sample during discharge are shown in Fig. 5a. Due to the significant overlapping of different CT processes, the EIS data has been interpreted

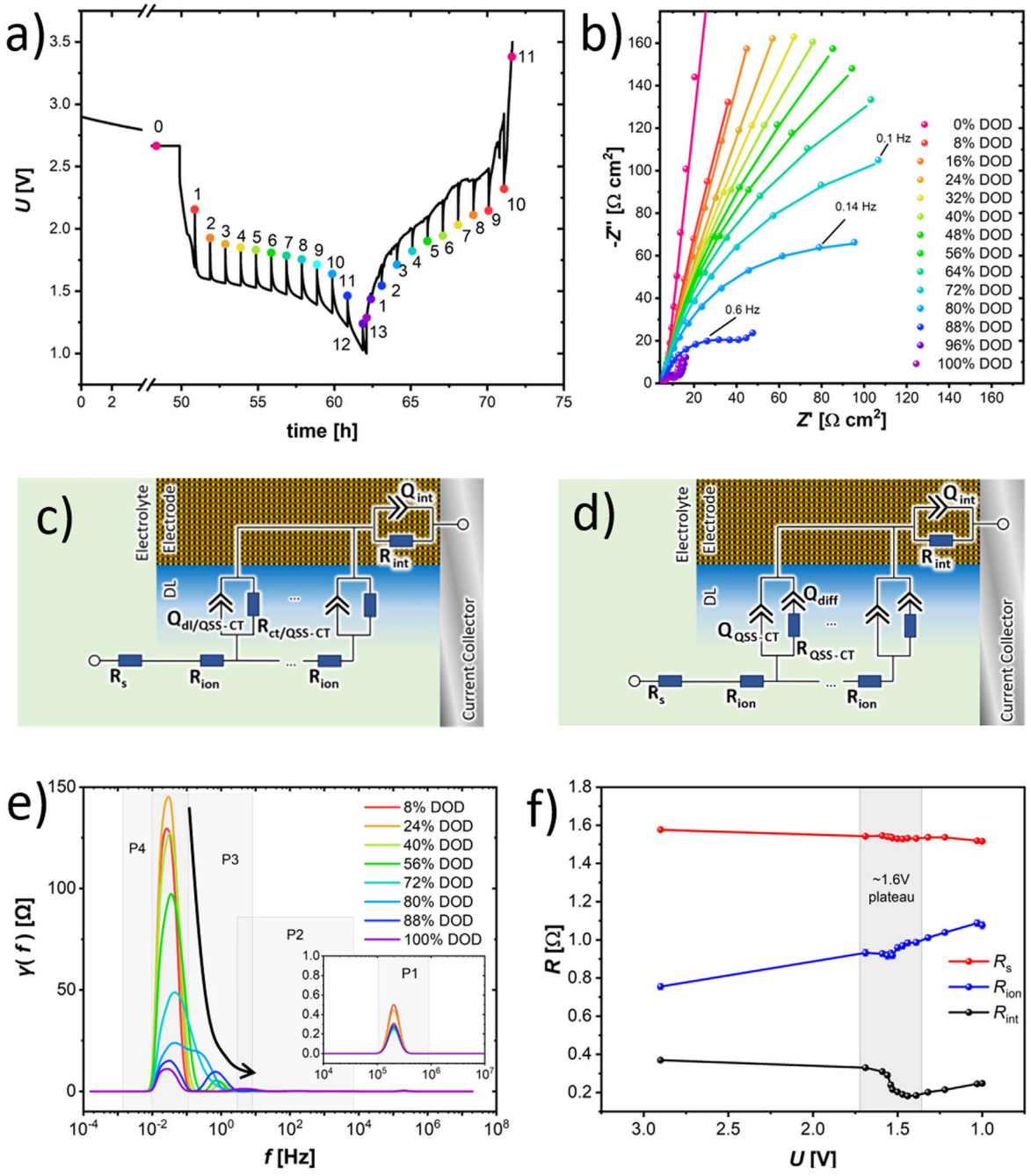

Figure 3. Cycling of CA(Ar)/S_{gas} symmetric cell: (a) Voltage profile; (b) Discharge impedance recordings in Nyquist presentation; scatter: measured data, line: fitting result; (c) and (d) ECs used for fitting OCV and discharge impedance recordings; (e) DRT spectra of discharge EIS recordings, for P1–P4 please see Table I; (f) Evolution of resistances during discharge; relative errors of fitted parameter < 2.3% (<6% for R_{int}).

by means of DRT analysis, see Fig. S8a. The influences can be attributed to the various, complex reactions taking place inside the cell during PS reduction. While in OCV phase the expected TLM with blocking conditions is visible, a MF semicircle arises shortly after starting the discharge process, see Fig. 5a, DOD = 17%. With regard to the discharge profile, EIS measurement 1 at 17% DOD was recorded at the 2.3 V plateau. Thus, the spectrum represents the impedance response of the first discharge plateau at which the dissolution of solid S (PS-CT_2) occurs and where no distinct ionic pore resistance contribution is evident. Instead, a semicircle superimposes the relevant frequency region. Moreover, the transformation of the LF branch toward a semicircle indicates that another process has already initiated. With further discharge and reaching the plateau at 2.1 V where the process $S_4^{2-} \rightarrow Li_2S_2/Li_2S$ (PS-CT_3) is dominated, the semicircle at LF becomes visible. The assignment of the appearing LF semicircle to PS-CT_3 is corroborating with the early growth of the HF semicircle which indicates a greater inter-particle resistance induced by deposition of reduction product at the surface, similarly observed upon solid reaction in previous discussed samples. Preceding aforementioned, for the first discharge EIS spectrum at DOD = 17%, fitting was performed with a serial combination of three (*RQ*)-elements and a series resistance depicting the ohmic resistances, see Fig. 5b. The following EIS spectra from 34% to 68% DOD, recorded at the plateau are fitted employing an EC illustrated in Fig. 3c as well, where the increase of the (*RQ*)-element describing the PS-CT_3 is increasing with time at the plateau.

Interestingly, distinct behavior can be found for the discharge impedance data at 85% and 100% DOD where the discharge plateau is already exceeded. Naturally, the CT resistance of the

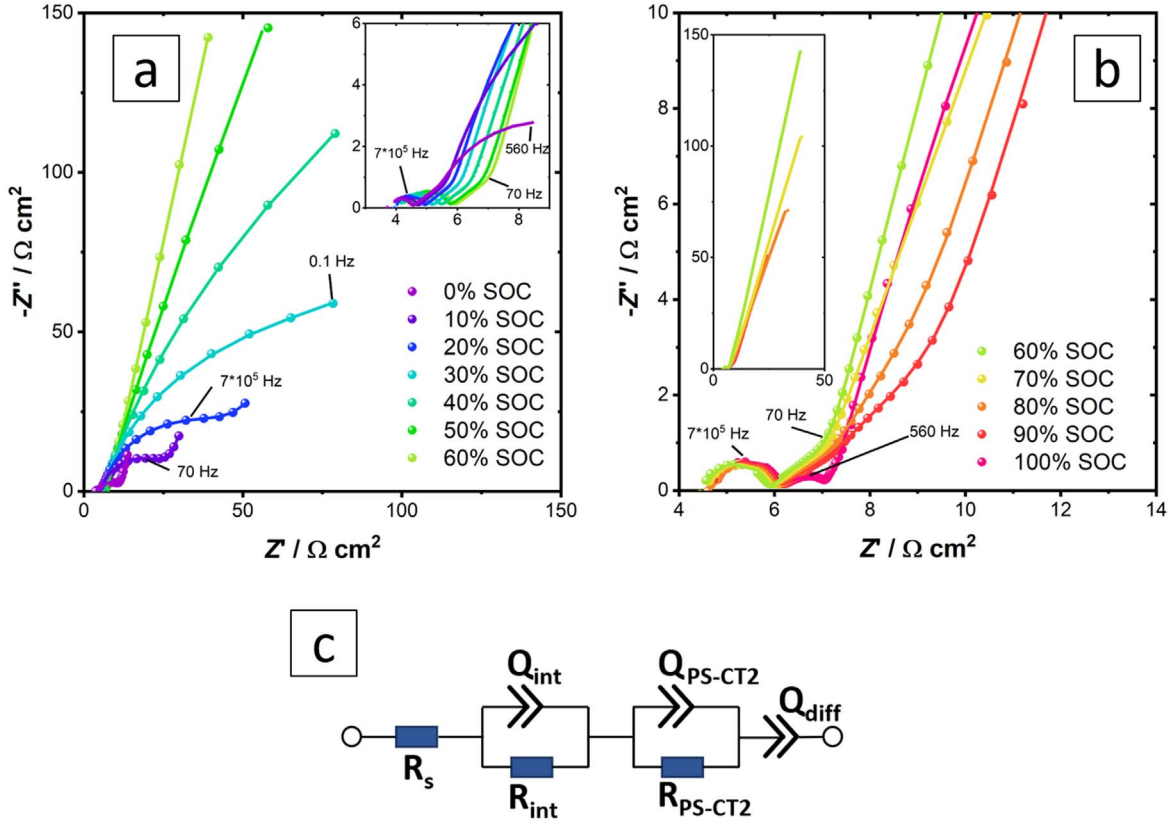

Figure 4. Charging of CA(Ar)/S_{gas} symmetric cell; (a) and (b) Impedance spectra at various SOCs; scatter: measured data, line: fitting result; (c) EC used for fitting later charge impedance recordings.

Li_2S_2/Li_2S-forming reduction steps is not detectable anymore given the absence of the formation of respective phase. However, a new individual process starts to appear at frequencies of 5 kHz $\leqslant f \leqslant$ 0.5 MHz, which is even higher than frequencies corresponding to the porous response and dissolution of the (PS-CT_2). The origin of this puzzling process is not fully clear. This relatively fast process on one hand could be assigned to the reduction of remaining high order PSs ($S_8^{2-} \rightarrow S_4^{2-}$ (PS-CT_1)) which fully occurs in liquid state, given the similar time-constant to the PS-CT_1 process for previous sample. Drvarič-Talian et al. reported a tendency for PSs to disproportionate resulting in the local depletion at cathode surface at deep discharge.[49] The depleted PS cannot be compensated fast enough by those PSs that are present in more distant areas, e.g. the separator, due to slow wandering. Hence, long-chain PSs are still present in the electrolyte, even though the discharge process has already continued to further reduction steps and fitting is performed with a blocking TLM with two serial (*RQ*)-elements, see Fig. 5c. On the other hand, an additional plausible interpretation of (*RQ*)-element appearing at lower DODs is the partial coating of the cathode surface during the formation of Li_2S. Diffusion of Li ions through such a coating layer could result in this additional resistance.

Herein, charging was finished faster than discharging and only four impedance spectra could be recorded, which indicates the loss of active material. For the first two spectra at 32% and 64% SOC recorded in the known 2.3 V charge plateau, the corresponding oxidation reaction Li_2S/$Li_2S_2 \rightarrow S_4^{2-}$ (PS-CT_3) as well as the solid diffusion branch can be observed in the LF region, see Fig. 5d. The ionic pore response in the MF part is superimposed by a distorted, enlarged semicircle shape, indicating two processes with similar relaxation times. With regard to the frequency range and previous information gained by investigation of the discharge spectra, the two MF impedance responses depict most likely oxidation reactions of long-chained PSs, hence $S_4^{2-} \rightarrow S_8^{2-}$ (PS-CT_1) and $S_8^{2-} \rightarrow S_8$ (PS-CT_2). For later charge impedance spectra at approximately 96% and 100% DOD, blocking behavior is observed. The porous response is still partially superimposed by PS-CT_1 apparent from DRT analysis (Fig. S8b), therefore a serial connection of (*RQ*)-circuits depicting the identified processes are chosen as EC, see Fig. 5e for the first and second charge EIS spectrum and Fig. 5f for later spectra.

Mixed CA(Ar)/S.—Subsequently, the impedance evolution of mixed, i.e. non-infiltrated, CA(Ar)/$S_{mixed,30}$ electrode upon first cycle where the characteristics of both kind of CT processes, i.e. PS-CT and QSS-CT, are evident is investigated. In order to maintain comparable conditions a S fraction of 30 wt% is chosen, since the S content of CA(Ar)/S_{gas} is usually around 20%–30%, see Fig. S9. Observation of impedance spectra recorded during OCV shows a decrease in the LF branch which could indicate a slight self-discharge, see Fig. S10, in contrary to CA(Ar)/S_{gas}. The recorded discharge impedance spectra are shown in Fig. 6. As observed before, the impedance response of the ionic pore resistance is superimposed by process PS-CT_2 ($S_8 \rightarrow S_8^{2-}$), Fig. 6a. A further semicircle in the LF area can be observed, which increases toward the end of the first discharge plateau at 48% DOD. This behavior is linked to the reduction of $S_4^{2-} \rightarrow Li_2S_2$/$Li_2S$ (PS-CT_3).

Simultaneously with the decrease of the LF arc and appearance of the solid-state process, the HF inter-particle response increases analogous to CA(Ar)/S_{gas} sample. Starting from EIS measurement 6 at 60% DOD, the porous characteristics (45° slope) become visible again in the EIS spectra, see Fig. 6b. In the second discharge plateau, the impedance evolution is similar to spectra of the gas infiltrated CA(Ar)/S cell. The LF branch drops toward the real axis and a semicircle shape becomes apparent.

The distinct presence of both CT mechanisms leads to a more complicated identification of the corresponding responses in the charge impedance data, which are shown in Fig. S11. However, since QSS-CT and PS-CT are dominant in different voltage areas, a

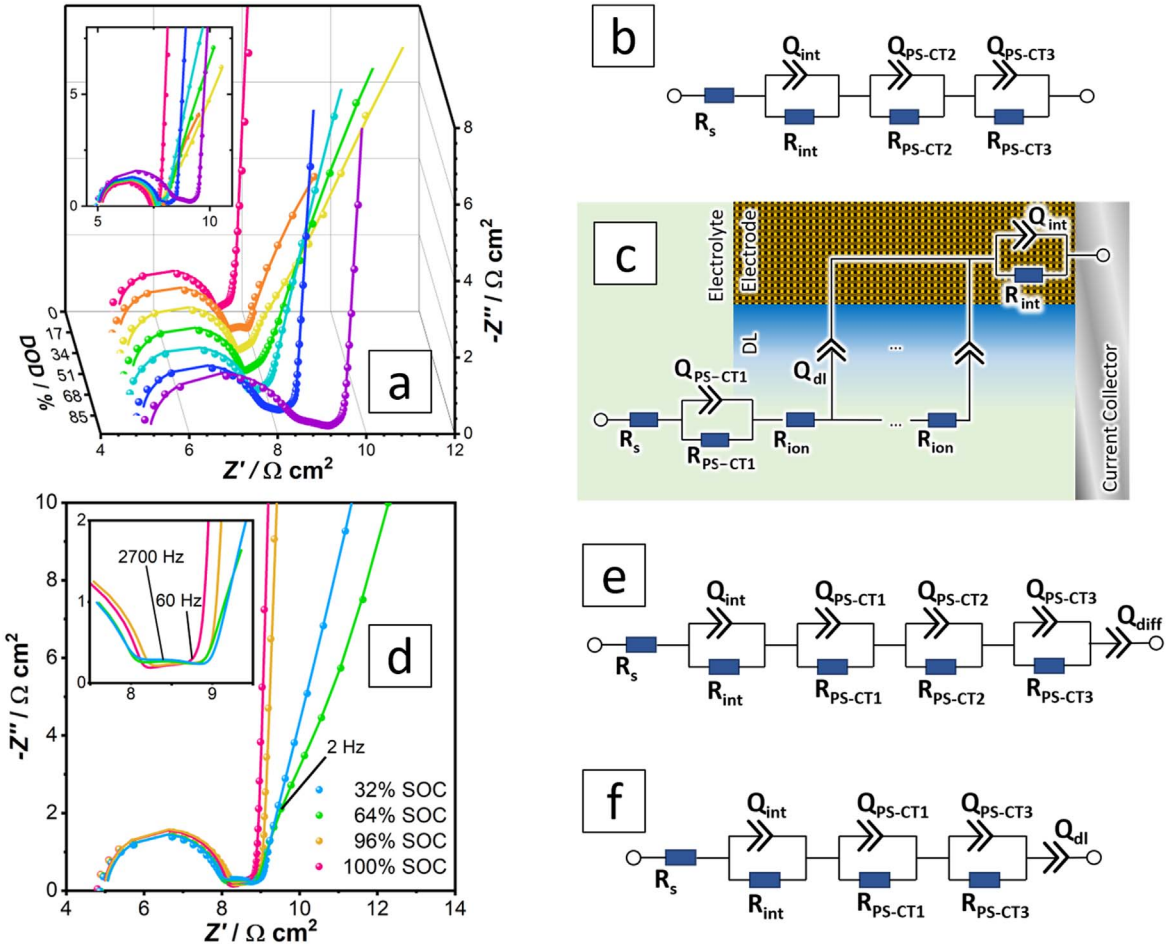

Figure 5. Cycling of KB/$S_{mixed,30}$ symmetrical cell; (a) Nyquist presentation of recorded impedance spectra during discharging; scatter: measured data, line: fitting result; (b) and (c) ECs used for fitting of discharge EIS data; (d) Nyquist presentation of recorded impedance spectra during charging; (e) and (f) ECs used for fitting of charge EIS data.

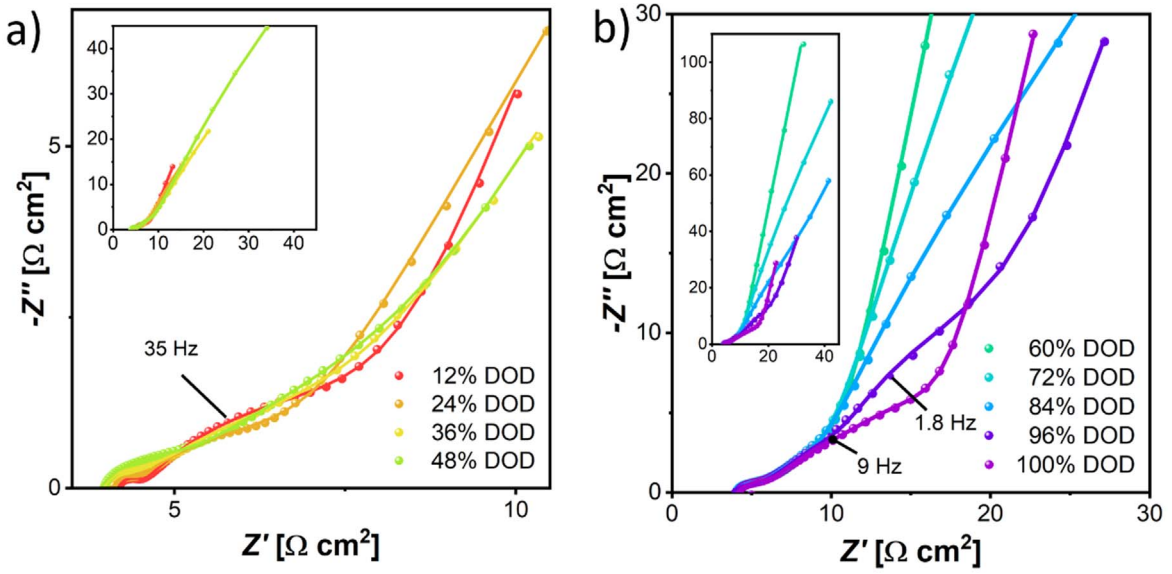

Figure 6. Discharge impedance data of CA(Ar)/$S_{mixed,30}$ symmetrical cell: (a) At early states showing PS-CT; (b) At later states showing QSS-CT; scatter: measured data, line: fitting result.

simultaneous occurrence is not expected. Hence, modelling and fitting can be achieved by applying the already known TLM as depicted in Fig. 3d.

All the above discussed processes occurring within cathodes in this study are listed in Table I. The QSS-CT has slower kinetics than the PS-based CT reactions which is mainly due to the limited

diffusion within the S particles compared to the fast PS disproportionation steps in solution.[43,51] Among the PS-based CT mechanisms, the PS-CT_1 reaction which occurs fully in the liquid state owns the lowest relaxation time constants.

The quantified R_{ct} values for the CA(Ar)/S_{gas} and KB/$S_{mixed,30}$ cathodes and their evolution at the main discharge plateau are depicted in Figs. 7a and 7b. The QSS-CT owns greater R_{ct} values due to the less exothermic reaction of $S_8 \rightarrow Li_2S$ compared to PS-based reduction steps.[45] Additionally, the confinement of S in the ultramicropores and lack of contact between electrolyte and active material calls for the solid-state diffusion of ions which leads to overpotentials as well.[43]

Interestingly, while $R_{QSS\text{-}CT}$ in the case of CA(Ar)/S_{gas} cathode decreases upon discharge at the plateau, the resistance of the PS-CT_3 mechanism occurring in the KB/$S_{mixed,30}$ cell appears to rise. The opposing trends can be explained with the dominating limiting factor of the different CT mechanisms. Since the QSS-CT mechanism reacts only in the solid phase, it is predominantly controlled by the diffusion of the Li-ions in the cathode. Even though both species, elemental S_8 as well as Li_2S, are generally considered to be insulating, the final discharge product Li_2S shows to have a greater ionic conductivity than elemental S_8 ($\sigma_{Li2S} = 1{\cdot}10^{-17}$ S cm^{-1} [50] vs $\sigma_{S8} = 5{\cdot}10^{-30}$ S cm^{-1} [50]). Hence, with ongoing discharge process the overall ionic conductivity in the C/S compound cathode grows whereby the diffusion and CT are facilitated. For PS-based CT mechanisms in Li/S cells, CT is mainly controlled by the surface reactions which occur at the three-phase boundary between the PS solution, insulating lithium sulfides precipitates and conductive C. With further discharge a growing amount of insulating Li_2S_2/Li_2S precipitation covers the conductive C surface (evident from the EIS data as discussed) which suppresses the further nucleation and growth of reduction products resulting in an increased CT resistance. Such passivation of the surface by final products of PS-based reduction reaction and increase in CT resistance at plateau is analogously observed and discussed using in situ TEM.[52]

Effect of electrolyte.—The combination of gas infiltration and microporous C enables the application of carbonate-based electrolyte whereby the excessive nucleophilic reaction of the carbonate solvent with the short-chain S-anions could be suppressed. Thereby, great specific discharge capacities can be obtained, see Figs. S4b. To assess the implementation of carbonate-based electrolytes within Li/S batteries employing a S infiltrated UMC host, the evolution of the EIS upon first cycle is compared to the ether-based electrolyte, see Figs. 8a. The observed EC/DMC cell was assembled using CA(Ar)/S_{gas} cathodes in a symmetrical cell configuration and with cycling parameter analogous to previous investigations executed for ether-based electrolytes. In the voltage profile, the elimination of the 2.1 V voltage plateau in contrary to the ether-electrolyte has been fully achieved. This is originated in the formation of a passivation layer on the cathode in contact with the carbonate electrolyte whereby the S is fully trapped within the carbon matrix.[17] Figure 8a shows the impedance data recorded during the initial OCV phase as well as the complete first cycle in a 3D Nyquist plot. For the carbonate-based electrolyte, in addition to the LF contributions (CT and the solid diffusion) a second semicircle can be observed in the MF region (50 Hz $\leqslant f \leqslant$ 0.5 MHz). This MF process which superimposes the ionic pore response appears to grow while discharging the cell. Figure 8b compares the EIS spectra recorded at the end of the discharge process of CA(Ar)/S_{gas} cells using DOL/DME (blue) and EC/DMC (black). During charging of the cell, a reversed progress of the QSS-CT response in the LF area can be observed. However, the MF semicircle is still growing while charging the cell and still visible at the end of the charging process, see Fig. 8c. This process is assigned to the passivation film to be known forming on the S cathode in contact with the carbonate electrolyte. The irreversibility of the process upon charge corroborates this assumption. Interestingly, the formation of such film on the cathode leads to an increase in the CT resistance (QSS-CT).

Conclusions

In the presented study, porous C-based S electrodes are systematically investigated using EIS. By applying symmetrical cell configuration, the contribution of the Li metal anode can be eliminated. Various C materials are used for this purpose, including commercially available KB and two micro- and micro-mesoporous CAs with different pore size distributions. The herein prepared composite cathodes indicate porous impedance response at the OCV. Therefore, TLMs are employed to thoroughly understand and evaluate the underlying processes including the porous characteristics of the cathode materials. Taking EIS and related processes into account, the overall impedance response of a porous C/S composite cathode at the OCV could be collectively described by an EC comprised of the following elements: bulk electrolyte resistance, electrolyte resistance in the pores, interparticle contact resistance and CT resistance at the electrode/electrolyte interface parallelly connected to the double layer capacitance.

To identify the plausible physical as well as underlying chemical and electrochemical processes appearing in impedance response of C/S composite cathodes upon cycling, three differently prepared composite cathodes (CA(Ar)/S_{gas}, KB/$S_{mixed,30}$ and CA(Ar)/$S_{mixed,30}$) are considered as model systems. These model systems represent specifically the common galvanostatic cycling behavior and the possible redox reaction mechanism in a Li-S cell. Considering the information derived from the recorded impedance data and extracted DRT spectra at different DODs in combination with voltage profile upon galvanostatic cycling in addition to the physical processes contributing to the overall impedance, individual CT reactions and their relaxation times are identified. Expectedly, the most sluggish CT process found is the QSS-CT process observed for the gas infiltrated ultramicroporous CA only appearing at deeper DODs. Unlike gas infiltrated CAs, the cathodes prepared using mechanical mixing reveal other CT processes with substantial lower relaxation time constants and faster kinetics. These faster CT reactions are assigned to the long- and short-chain PS reduction in

Table I. Simplified identified processes and their frequency range and relaxation time.

Process	Reaction	Frequency Range f	Relaxation time τ
P1	Inter-particle response	0.1 MHz $\leqslant f \leqslant$ 1 MHz	8e-7 s
P2	Ionic pore resistance	5 Hz $\leqslant f \leqslant$ 10 kHz	
P3	QSS-CT	0.01 Hz $\leqslant f \leqslant$ 10 Hz	5e-2 s
P4	Solid diffusion	$f <$ 1 Hz	
P5	PS-CT_1: $S_8^{2-} \leftrightarrow S_4^{2-}$	5 kHz $\leqslant f \leqslant$ 0.5 MHz	8e-5 s
P6	PS-CT_2: $S_8 \leftrightarrow S_8^{2-}$	1 Hz $\leqslant f \leqslant$ 10 kHz	1e-3 s
P7	PS-CT_3: $S_4^{2-} \leftrightarrow Li_2S_2/Li_2S$	1 Hz $\leqslant f \leqslant$ 50 Hz	8e-2 s

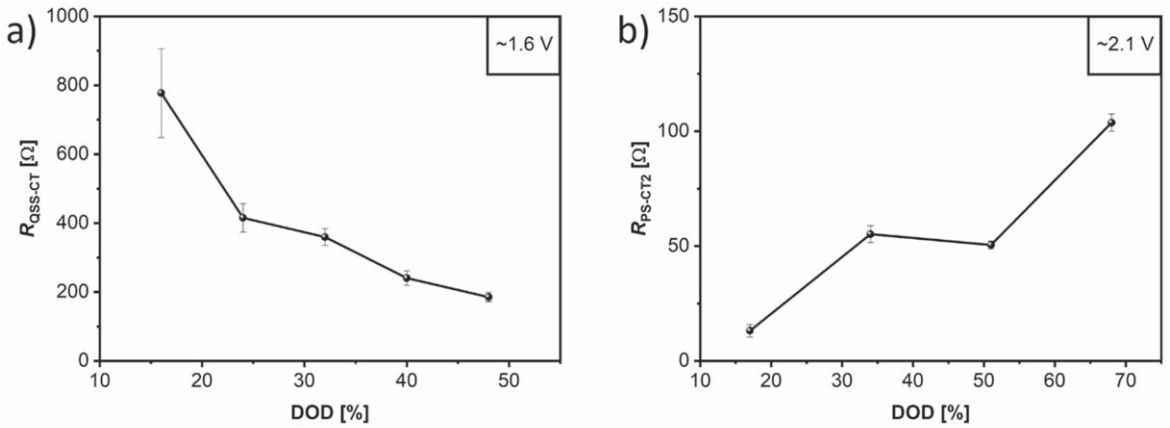

Figure 7. Comparison of the CT resistances of the main processes on their plateaus of (a) CA(Ar)/S_{gas} and (b) KB/$S_{mixed,30}$.

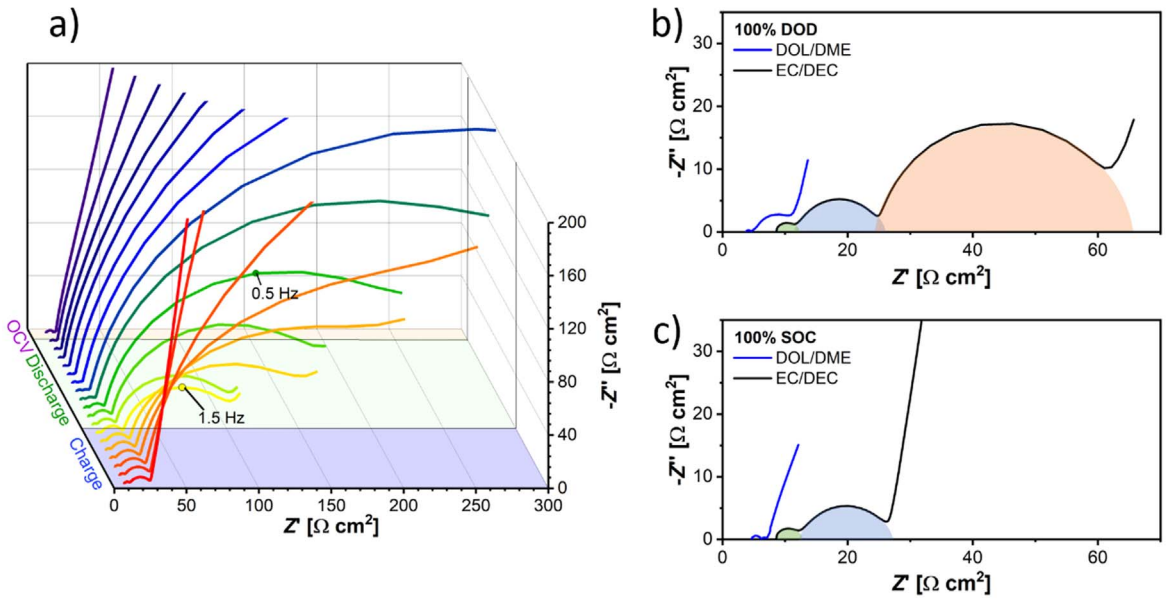

Figure 8. (a) Recorded impedance spectra at various DODs/SOCs for CA(Ar)/S_{gas} symmetrical cell with carbonate-based electrolyte; comparison of ether- and carbonate-based electrolyte; (b) Last discharge EIS spectrum; (c) Last charge EIS spectrum.

the solution phase. Among these PS-CTs, the smallest time constant, i.e. the fastest kinetic, is derived for PS-CT_1: $S_8^{2-} \leftrightarrow S_4^{2-}$, the reduction step which fully occurs in liquid phase. The solution of solid S in the electrolyte, PS-CT_2: $S_8 \leftrightarrow S_8^{2-}$ has similar relaxation times to that of the porous response, resulting in an overlap in the impedance spectra. Therefore, it could be concluded that the lack of porous response for the C/S composite cathode implies the dissolution of PSs. For the OCV particularly, this absence is likely to be an indicator of self-discharge. An additional process observed at 2.1 V plateau is attributed to the relatively slow PS-CT_3: $S_4^{2-} \leftrightarrow Li_2S_2/Li_2S$. Although in this study the transmission line theory is mainly used to describe the porous properties of cathode materials, the large number of processes with similar relaxation times called for extended TLMs or connections of different ECs for single responses in series. For carbonate-based electrolytes, an additional process in the MF regime growing upon charge and discharge is observed which is assigned to the passivation film forming on the S cathode exposed to such electrolytes. In summary, this work successfully identified the implication of different plausible processes and phenomena related to the composite C/S cathode in the recorded impedance spectra.

Acknowledgments

The authors thank Dr. Marina Schwan and Jessica Schettler at the institute of material research (DLR) in cologne for providing the carbon aerogels for this study.

ORCID

Martina Gerle https://orcid.org/0000-0003-2492-8367
Norbert Wagner https://orcid.org/0000-0002-2596-8689
Joachim Häcker https://orcid.org/0000-0003-2031-9898
Maryam Nojabaee https://orcid.org/0000-0001-5225-3526
Kasper Andreas Friedrich https://orcid.org/0000-0002-2968-5029

References

1. A. Fotouhi, D. J. Auger, L. O'Neill, T. Cleaver, and S. Walus, *Energies*, **10**, 1937 (2017).
2. S. Sripad and V. Viswanathan, *ACS Energy Lett.*, **2**, 1669 (2017).
3. A. Manthiram, Y. Fu, and Y.-S. Su, *Acc. Chem. Res.*, **46**, 1125 (2013).
4. J. B. Robinson et al., *J. Phys.: Energy*, **3**, 031501 (2021).
5. P. Barai, A. Mistry, and P. P. Mukherjee, *Extreme Mech. Lett.*, **9**, 359 (2016).
6. R. Elazari, G. Salitra, Y. Talyosef, J. Grinblat, C. Scordilis-Kelley, A. Xiao, J. Affinito, and D. Aurbach, *J. Electrochem. Soc.*, **157**, A1131 (2010).

7. X. He, J. Ren, L. Wang, W. Pu, C. Jiang, and C. Wan, *J. Power Sources*, **190**, 154 (2009).
8. C. Zhao, G. L. Xu, T. Zhao, and K. Amine, *Angew. Chem. Int. Ed.*, **59**, 17634 (2020).
9. A. Manthiram, S.-H. Chung, and C. Zu, *Adv. Mater.*, **27**, 1980 (2015).
10. H. Althues, S. Dörfler, S. Thieme, P. Strubel, and S. Kaskel, "Sulfur Cathodes." *Lithium–Sulfur Batteries*, ed. M. Wild and G. Offer (Wiley, Hoboken, NJ) p. 33 (2019).
11. C. Kensy, F. Schwotzer, S. Dörfler, H. Althues, and S. Kaskel, *Batteries Supercaps*, **4**, 823 (2021).
12. W. Zhou, B. Guo, H. Gao, and J. B. Goodenough, *Adv. Energy Mater.*, **6**, 1502059 (2016).
13. D. Eroglu, K. R. Zavadil, and K. G. Gallagher, *J. Electrochem. Soc.*, **162**, A982 (2015).
14. A. Eftekhari and D.-W. Kim, *J. Mater. Chem. A*, **8**, 1485 (2020).
15. L. Borchardt, M. Oschatz, and S. Kaskel, *Cemistry - A European Journal*, **22**, 7324 (2016).
16. S. Xin, L. Gu, N.-H. Zhao, Y.-X. Yin, L.-J. Zhou, Y.-G. Guo, and L.-J. Wan, *J. Am. Chem. Soc.*, **134**, 18510 (2012).
17. M. Nojabaee, B. Sievert, M. Schwan, J. Schettler, F. Warth, N. Wagner, B. Milow, and K. A. Friedrich, *J. Mater. Chem. A*, **9**, 6508 (2021).
18. M. Helen, T. Diemant, S. Schindler, R. J. Behm, M. Danzer, U. Kaiser, M. Fichtner, and M. Anji Reddy, *ACS Omega*, **3**, 11290 (2018).
19. E. Markevich, G. Salitra, A. Rosenman, Y. Talyosef, F. Chesneau, and D. Aurbach, *Electrochem. Commun.*, **60**, 42 (2015).
20. J. Tan, D. Liu, X. Xu, and L. Mai, *Nanoscale*, **9**, 19001 (2017).
21. N. A. Cañas, S. Wolf, N. Wagner, and K. A. Friedrich, *J. Power Sources*, **226**, 313 (2013).
22. Q. He, A. T. S. Freiberg, M. U. M. Patel, S. Qian, and H. A. Gasteiger, *J. Electrochem. Soc.*, **167**, 080508 (2020).
23. M. U. M. Patel and R. Dominko, *Chem. Sus. Chem*, **7**, 2167 (2014).
24. J. Nelson, S. Misra, Y. Yang, A. Jackson, Y. Liu, H. Wang, H. Dai, J. C. Andrews, Y. Cui, and M. F. Toney, *J. Am. Chem. Soc.*, **134**, 6337 (2012).
25. Y. X. Song, Y. Shi, J. Wan, B. Liu, L. J. Wan, and R. Wen, *Adv. Energy Mater.*, **10**, 2000465 (2020).
26. Y.-C. Chien, A. S. Menon, W. R. Brant, D. Brandell, and M. Lacey, *J. Am. Chem. Soc.*, **142**, 1449 (2019).
27. V. S. Kolosnitsyn, E. V. Kuz'mina, E. V. Karaseva, and S. E. Mochalov, *Russ. J. Electrochem.*, **47**, 793 (2011).
28. N. A. Canas, K. Hirose, B. Pascucci, N. Wagner, K. A. Friedrich, and R. Hiesgen, *Electrochim. Acta*, **97**, 42 (2013).
29. L. Yuan, X. Qiu, L. Chen, and W. Zhu, *J. Power Sources*, **189**, 127 (2009).
30. S. Walus, C. Barchasz, R. Bouchet, and F. Alloin, *Electrochim. Acta*, **359**, 136944 (2020).
31. C. Bünzli, H. Kaiser, and P. Novák, *J. Electrochem. Soc.*, **162**, A218 (2014).
32. J. Song, H. Lee, Y. Wang, and C. Wan, *J. Power Sources*, **111**, 255 (2002).
33. A. Martinent, B. Le Gorrec, C. Montella, and R. Yazami, *J. Power Sources*, **97**, 83 (2001).
34. R. De Levie, *Electrochim. Acta*, **8**, 751 (1963).
35. R. De Levie, *Electrochim. Acta*, **9**, 1231 (1964).
36. J. Bisquert, G. Garcia-Belmonte, F. Fabregat-Santiago, and A. Compte, *Electrochem. Commun.*, **1**, 429 (1999).
37. J. Bisquert, *Phys. Chem. Chem. Phys.*, **2**, 4185 (2000).
38. M. Adamič, S. Drvarič-Talian, A. R. Sinigoj, I. Humar, J. Moškon, and M. Gaberšček, *J. Electrochem. Soc.*, **166**, A5045 (2019).
39. S. Drvarič-Talian, J. Bobnar, A. R. Sinigoj, I. Humar, and M. Gaberšček, *J. Phys. Chem. C*, **123**, 27997 (2019).
40. M. Urquidi-Macdonald, S. Real, and D. D. Macdonald, *Electrochim. Acta*, **35**, 1559 (1990).
41. J. Landesfeind, J. Hattendorff, A. Ehrl, W. A. Wall, and H. A. Gasteiger, *J. Electrochem. Soc.*, **163**, A1373 (2016).
42. Q. Wang, J. Zheng, E. Walter, H. Pan, D. Lv, P. Zuo, H. Chen, Z. D. Deng, B. Y. Liaw, and X. J. J. O. T. E. S. Yu, *J. Electrochem. Soc.*, **162**, A474 (2015).
43. C.-P. Yang, Y.-X. Yin, Y.-G. Guo, and L.-J. Wan, *J. Am. Chem. Soc.*, **137**, 2215 (2015).
44. S. Walus, "Lithium Sulfide." *Lithium-Sulfur Batteries*, ed. M. Wild and G. Offer (Wiley, Hoboken, NJ) p. 147 (2019).
45. S. Tsuzuki, T. Kaneko, K. Sodeyama, Y. Umebayashi, W. Shinoda, S. Seki, K. Ueno, K. Dokko, and M. Watanabe, *Phys. Chem. Chem. Phys.*, **23**, 6832 (2021).
46. S. Walus, C. Barchasz, R. Bouchet, J. Martin, J. Lepretre, and F. Alloin, *Electrochim. Acta*, **180**, 178 (2015).
47. Z. Li, L. Yuan, Z. Yi, Y. Sun, Y. Liu, Y. Jiang, Y. Shen, Y. Xin, Z. Zhang, and Y. Huang, *Adv. Energy Mater.*, **4**, 1301473 (2014).
48. Z. Deng, Z. Zhang, Y. Lai, J. Liu, J. Li, and Y. Liu, *J. Electrochem. Soc.*, **160**, A553 (2013).
49. S. Drvarič-Talian, G. Kapun, J. Moškon, A. Vizintin, A. Randon-Vitanova, R. Dominko, and M. Gaberšček, *Chem. Mater.*, **31**, 9012 (2019).
50. C. Deng, Z. Wang, S. Wang, and J. Yu, *J. Mater. Chem. A*, **7**, 12381 (2019).
51. Y. Wang, T. Liu, L. Estevez, and J. Kumar, *Energy Storage Mater.*, **27**, 232 (2020).
52. Z.-L. Xu, S. J. Kim, D. Chang, K.-Y. Park, K. S. Dae, K. P. Dao, J. M. Yuk, and K. Kang, *Energy Environ. Sci.*, **12**, 3144 (2019).